

Phonon angular momentum Hall effect

Sungjoon Park^{1,2,3} and Bohm-Jung Yang^{2,1,3,*}

¹Center for Correlated Electron Systems, Institute for Basic Science (IBS), Seoul 08826, Korea

²Department of Physics and Astronomy, Seoul National University, Seoul 08826, Korea

³Center for Theoretical Physics (CTP), Seoul National University, Seoul 08826, Korea

(Dated: May 17, 2022)

We show that temperature gradient can cause a transverse flow of phonon angular momentum. This intrinsic effect relies only on the presence of transverse and longitudinal acoustic phonons, and is therefore, ubiquitous in condensed matter systems. The phonon angular momentum Hall current creates asymmetric angular momentum distribution in a crystal with edges. When the atoms in the crystal carry nonzero Born effective charge, the phonon angular momentum accumulated at the edges creates asymmetric distribution of magnetization in a crystal with edges.

PACS numbers:

Transverse responses of materials to external forces, generally known as Hall effects, have played quintessential roles in the advance in fundamental physics [1, 2]. For instance, when external electric field is applied to a conductor, electric current can flow in the transverse direction, which is known as the anomalous Hall effect [1, 3–5]. Similarly, spin and orbital angular momenta can flow in the direction transverse to the electric field, leading to the spin [2, 6–11] and orbital Hall effects [12], respectively. The intrinsic mechanisms for the various Hall effects [3, 8, 9, 12] are of particular interest as they do not rely on scattering mechanisms and are closely related to topological phases such as Chern insulators [13] and quantum spin Hall insulators [14, 15]. Moreover, the manipulation of the charge, spin, and orbital degrees of freedom by Hall effects facilitates efficient device engineering based on functional materials [16, 17].

Hall effects can occur not only in conductors but also in insulators that generally do not respond well to external electric field because of the frozen charge degrees of freedom. Here, the key idea is that temperature gradient can apply a statistical force to the quasiparticles in insulators, such as magnon and phonon, in a manner analogous to the electric field in a conductor. For example, when a temperature gradient is applied, heat current can flow in the transverse direction to the temperature gradient through the low-energy charge-neutral excitations such as magnon [18–20], phonon [21–24], and magnetoelastic excitations [25, 26]. This so-called thermal Hall effect can be viewed as the thermal counterpart of the anomalous Hall effect. The spin Hall effect also has a thermal analogy, known as the spin Nernst effect, in which magnons [27, 28] or magnetoelastic excitations [29, 30] transport spins in the direction transverse to the thermal gradient.

In this work, we add a new item to the list of Hall effects, which we call the phonon angular momentum Hall effect (PAMHE) wherein the phonon angular momentum (PAM) flows transversely to the temperature gradient. By PAM, we refer to the angular momentum carried by atoms in a lattice as they vibrate with respect to their equilibrium position with displacement $\mathbf{u}_\alpha(\mathbf{R})$ and momentum $\mathbf{p}_\alpha(\mathbf{R})$, as shown in Fig. 1 (a). Here, α is the sublattice index and \mathbf{R} denotes the posi-

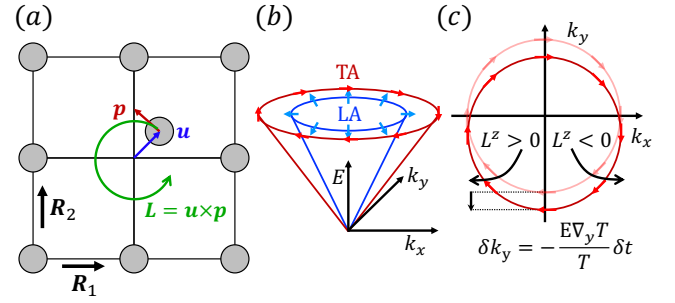


FIG. 1: (a) Illustration of the phonon angular momentum (PAM) in a square lattice. (b) Transverse and acoustic phonon energy spectra and their polarization vectors, which are indicated by arrows. (c) Shift of the transverse acoustic phonon states at a fixed energy E by $\delta \mathbf{k}$ under the application of thermal gradient, and their subsequent dynamics.

tion of a unit cell, so that the equilibrium position of an atom in the unit cell at \mathbf{R} with sublattice α is given by $\mathbf{R} + \delta_\alpha$. For convenience, we rescale the displacement (momentum) by multiplying (dividing) it by the square root of its mass. The PAM is then given by [31–34] $\mathcal{L} = \sum_{\mathbf{R}, \alpha} \mathbf{u}_\alpha(\mathbf{R}) \times \mathbf{p}_\alpha(\mathbf{R})$. Defining $\mathbf{x}_\alpha(\mathbf{R}) = (\mathbf{p}_\alpha(\mathbf{R}), \mathbf{u}_\alpha(\mathbf{R}))$ and taking the Fourier transformation $\mathbf{x}_{\mathbf{k}\alpha} = \frac{1}{\sqrt{V}} \sum_{\mathbf{R}} \mathbf{x}_\alpha(\mathbf{R}) e^{-i\mathbf{k} \cdot (\mathbf{R} + \delta_\alpha)}$, we have

$$\mathcal{L} = \frac{1}{2} \sum_{\mathbf{k}, \alpha} \mathbf{x}_{-\mathbf{k}\alpha} \mathbf{L}_\alpha \mathbf{x}_{\mathbf{k}\alpha}, \quad (L^\rho)_\alpha = \begin{pmatrix} & -\ell_\rho \\ \ell_\rho & \end{pmatrix}. \quad (1)$$

Here, ℓ_ρ is a matrix whose components are $(\ell_\rho)_{\mu\nu} = \varepsilon_{\mu\nu\rho}$, where $\varepsilon_{\mu\nu\rho}$ is the Levi-Civita symbol and μ, ν, ρ run over x, y , and z . Note that the matrix $(L^\rho)_\alpha$ is independent of α .

To understand why PAMHE occurs, we consider the dynamics of phonon modes when thermal gradient is applied, as in Ref. [35], where the dynamics of electronic orbitals under electric field is considered. For simplicity, we first restrict the discussion to a two-dimensional elastic continuum, so that the

phonon Hamiltonian is given by

$$\mathcal{H} = \frac{1}{2} \sum_{\mathbf{k}} \mathbf{x}_{-\mathbf{k}} H_{\mathbf{k}} \mathbf{x}_{\mathbf{k}}, \quad H_{\mathbf{k}} = \begin{pmatrix} \tau_0 & 0 \\ 0 & D_{\mathbf{k}} \end{pmatrix}, \quad (2)$$

where $\mathbf{x}_{\mathbf{k}} = (\mathbf{p}_{\mathbf{k}}, \mathbf{u}_{\mathbf{k}})$, τ_0 is a 2×2 identity matrix defined in the space spanned by the x and y components of $\mathbf{p}_{\mathbf{k}}$ or $\mathbf{u}_{\mathbf{k}}$, and $D_{\mathbf{k}}^{\mu\nu} = v_T^2 k^2 + (v_L^2 - v_T^2) k_{\mu} k_{\nu}$ is the dynamical matrix. The corresponding Heisenberg's equation is $i \frac{\partial}{\partial t} \mathbf{x}_{\mathbf{k}}(t) = (\tau_0 \otimes \sigma^y) H_{\mathbf{k}} \mathbf{x}_{\mathbf{k}}(t)$, where σ^{μ} with $\mu = x, y, z$ are the Pauli matrices connecting $\mathbf{p}_{\mathbf{k}}$ and $\mathbf{u}_{\mathbf{k}}$. In the following, we omit τ_0 by writing σ^{μ} instead of $\tau_0 \otimes \sigma^{\mu}$. This equation has four normal modes $\mathbf{x}_{\mathbf{k},n}(t) = \chi_{\mathbf{k},n} e^{-iE_{\mathbf{k},n}t}$, where $\chi_{\mathbf{k},n} = \begin{pmatrix} -iE_{\mathbf{k},n} \epsilon_{\mathbf{k},n} \\ \epsilon_{\mathbf{k},n} \end{pmatrix}$ for $n = L, T, -L, -T$, and the polarization vector $\epsilon_{\mathbf{k},n}$ satisfies $D_{\mathbf{k}} \epsilon_{\mathbf{k},n} = E_{\mathbf{k},n}^2 \epsilon_{\mathbf{k},n}$. Explicitly, $\epsilon_{\mathbf{k},L} = \epsilon_{\mathbf{k},-L} = \frac{1}{k\sqrt{2E_{\mathbf{k},L}}} \begin{pmatrix} k_x \\ k_y \end{pmatrix}$ and $\epsilon_{\mathbf{k},T} = \epsilon_{\mathbf{k},-T} = \frac{1}{k\sqrt{2E_{\mathbf{k},T}}} \begin{pmatrix} k_y \\ -k_x \end{pmatrix}$ are longitudinal and transverse polarization vectors, respectively, with $E_{\mathbf{k},L} = -E_{\mathbf{k},-L} = v_L k$ and $E_{\mathbf{k},T} = -E_{\mathbf{k},-T} = v_T k$, as shown in Fig. 1 (b). Among the four normal modes, only two modes (one longitudinal mode and one transverse mode) are physically meaningful. For convenience, however, we use the 4×4 matrix formulation. We note that the polarization vectors are chosen so that the normalization $\chi_{\mathbf{k},m}^{\dagger} \sigma^y \chi_{\mathbf{k},n} = \delta_{mn}^z$ is satisfied, where $\delta_{nn}^z = 1$ (-1) for $n = L, T$ ($n = -L, -T$), while $\delta_{mn}^z = 0$ for $m \neq n$.

Because we restrict ourselves to two-dimensions, only L^z is meaningful, which is now a 4×4 matrix because $\mu, \nu = x, y$ in $(\ell^z)_{\mu\nu}$. For the normal modes, the expectation value of PAM is $\langle \mathcal{L}^z \rangle_{\mathbf{k},n}(t) = \mathbf{x}_{\mathbf{k},n}^{\dagger}(t) L^z \mathbf{x}_{\mathbf{k},n}(t) = 0$. However, phonon states can develop nonzero angular momentum when thermal gradient is applied, as we now explain. We first note that according to the method of pseudogravitational potential, the effect of thermal gradient can be treated by introducing a scalar potential $\phi(\mathbf{r})$ that couples to the energy E in the form ϕE , with $\nabla \phi = \frac{\nabla T}{T}$ [20, 36–38]. Thus, under the application of thermal gradient $(\nabla_y T) \hat{y}$ with $\nabla_y T > 0$ for time δt , states shift in the momentum space from \mathbf{k} to $\mathbf{k} + \delta \mathbf{k}$, where $\delta \mathbf{k} = (0, -\delta k_y)$ ($\delta k_y > 0$) and $\delta k_y = E \nabla \phi \delta t = \frac{E \nabla_y T}{T} \delta t$, as illustrated in Fig. 1 (c).

Now let us examine the effect of thermal gradient on the transverse modes. We note that, although $\chi_{\mathbf{k},T}$ is not an eigenmode after the momentum shift $\mathbf{k} \rightarrow \mathbf{k} + \delta \mathbf{k}$, it can be decomposed in terms of the eigenmodes at $\mathbf{k} + \delta \mathbf{k}$, as $\chi_{\mathbf{k},T} = \sum_n \alpha_n^T \chi_{\mathbf{k}+\delta \mathbf{k},n}$, where $\alpha_n^T = \delta_{nn}^z \chi_{\mathbf{k}+\delta \mathbf{k},n}^{\dagger} \sigma^y \chi_{\mathbf{k},T}$. Then, the evolution of $\chi_{\mathbf{k},T}$ for time t gives $\mathbf{x}_{\mathbf{k},T}^{\text{shift}}(t) = \sum_n e^{-itE_{\mathbf{k}+\delta \mathbf{k},n}} \alpha_n^T \chi_{\mathbf{k}+\delta \mathbf{k},n}$. Even though the normal modes have vanishing expectation value of PAM, the shifted states develop nonzero PAM $\langle \mathcal{L}^z \rangle_{\mathbf{k},T}^{\text{shift}}(t) = (\mathbf{x}_{\mathbf{k},T}^{\text{shift}})^{\dagger}(t) L^z \mathbf{x}_{\mathbf{k},T}^{\text{shift}}(t) \propto -k_x \delta k_y t$, to the lowest order in t and δk_y , as shown in detail in the Supplemental Materials (SM) [39]. Thus, the states with $k_x < 0$, which drift towards $-\hat{x}$, has positive expectation value of \mathcal{L}^z , while the states with $k_x > 0$, which drift towards \hat{x} , has negative expectation value of \mathcal{L}^z , so that there is a net movement of PAM towards $-\hat{x}$.

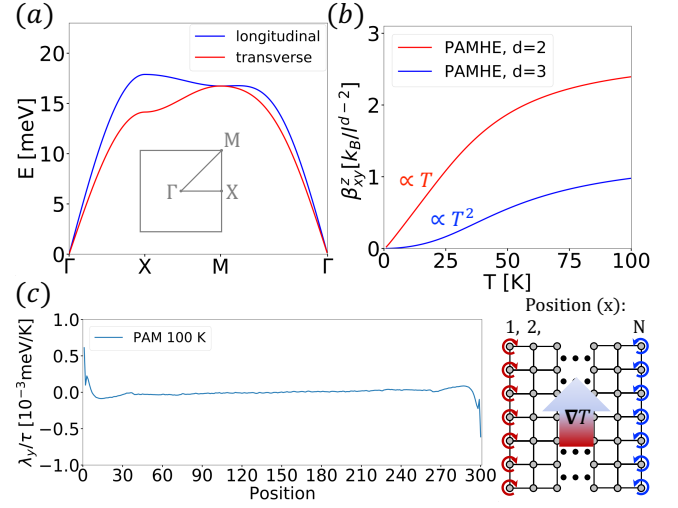


FIG. 2: (a) Phonon spectrum along the high symmetry lines for the square lattice, with the NN transverse and longitudinal spring constants ($k_T = 20$ (meV) 2 , $k_L = 50$ (meV) 2) and the NNN transverse and longitudinal spring constants ($k'_T = 10$ (meV) 2 , $k'_L = 20$ (meV) 2). (b) The PAM Hall conductivity with the parameters given in (a) for the square lattice (red line) and the cubic (blue line) lattice. In the y axis, d is the spatial dimension and l is the lattice constant. (c) Spatial distribution of PAM induced by temperature gradient for a square lattice with the geometry given on the right.

We note that for the longitudinal modes, the PAM flow is opposite in direction, but that their occupation is lower because the longitudinal modes carry higher energy than the transverse modes.

Lattice model— Let us demonstrate the idea of PAMHE developed up to now, by solving the Hamiltonian in Eq. (2) for a simple harmonic oscillator model on the square lattice in Fig. 1 (a). For simplicity, we only consider the longitudinal and transverse spring constants between the nearest neighbors (NN) and the next nearest neighbors (NNN) to obtain the dynamical matrix $D_{\mathbf{k}}$, whose explicit form is given in SM [39].

To diagonalize the Hamiltonian, we write $\mathbf{x}_{\mathbf{k}} = \sum_n \chi_{\mathbf{k},n} b_{\mathbf{k},n}$, where $n = 2, 1, -1, -2$ [24, 25]. Here, $b_{\mathbf{k},n}$ is the phonon annihilation operator satisfying $b_{\mathbf{k},n}^{\dagger} = b_{-\mathbf{k},-n}$, and $\chi_{\mathbf{k},n}$ is the phonon wavefunction satisfying $\sigma^y H_{\mathbf{k}} \chi_{\mathbf{k},n} = E_{\mathbf{k},n} \chi_{\mathbf{k},n}$, $\chi_{\mathbf{k},m}^{\dagger} \sigma^y \chi_{\mathbf{k},n} = \delta_{mn}$ and $\chi_{\mathbf{k},n}^* = \chi_{-\mathbf{k},-n}$. The eigenvalues satisfy $E_{\mathbf{k},n} \geq 0$ for $n > 0$, $E_{\mathbf{k},n} \leq 0$ for $n < 0$, and $E_{\mathbf{k},n} = -E_{-\mathbf{k},-n}$. Thus, $\mathcal{H} = \frac{1}{2} \sum_{\mathbf{k},n} b_{\mathbf{k},n}^{\dagger} b_{\mathbf{k},n} \delta_{nn} E_{\mathbf{k},n} = \sum_{\mathbf{k},n>0} b_{\mathbf{k},n}^{\dagger} b_{\mathbf{k},n} (E_{\mathbf{k},n} + \frac{1}{2})$. The energy spectrum is shown in Fig. 2 (a). The blue and the red lines are approximately longitudinal and transverse polarized, respectively, near the Γ point.

We next examine some properties of the PAM. First, the PAM is generally not conserved, i.e. $[\sigma^y L, H_{\mathbf{k}}] \neq 0$ [39]. Adopting the notation $|n, \mathbf{k}\rangle = \chi_{\mathbf{k},n}$, this implies $\langle m, \mathbf{k} | [\sigma^y L, H_{\mathbf{k}}] | n, \mathbf{k}\rangle = \langle m, \mathbf{k} | L | n, \mathbf{k}\rangle (E_{\mathbf{k},n} - E_{\mathbf{k},m}) \neq 0$ for some $m \neq n$. Thus, $\mathcal{L} = \frac{1}{2} \sum_{\mathbf{k},m,n} \langle m, \mathbf{k} | L | n, \mathbf{k}\rangle b_{\mathbf{k},m}^{\dagger} b_{\mathbf{k},n}$ has interband components

in the energy basis. Furthermore, the square lattice model has both inversion (\mathcal{P}) and time reversal (\mathcal{T}) symmetries. The actions of these symmetry operators on the energy eigenstates are given by $\mathcal{P}|n, \mathbf{k}\rangle = -|n, -\mathbf{k}\rangle$ and $\mathcal{T}|n, \mathbf{k}\rangle = -\sigma^z \mathcal{K}|n, -\mathbf{k}\rangle$, where \mathcal{K} is the complex conjugation operator. Thus, in the presence of $\mathcal{P}\mathcal{T}$ symmetry, $|n, \mathbf{k}\rangle = \sigma^z \mathcal{K}|n, \mathbf{k}\rangle$. Since $L\sigma^z = -\sigma^z L$ and $L^\dagger = L$, we have $\langle n, \mathbf{k}|L|n, \mathbf{k}\rangle = 0$, i.e. there are no intraband components. Note that the expectation value of the PAM in thermal equilibrium, that is, $\langle \mathcal{Z} \rangle_{\text{eq}}$, vanish in when there is time reversal symmetry.

To study the transport of PAM, we define the PAM current density in the μ direction by $j_\mu^{L^\rho} = \frac{1}{2V} \sum_{\mathbf{k}} \mathbf{x}_{-\mathbf{k}} \frac{L^\rho v_{\mathbf{k},\mu} + v_{\mathbf{k},\mu} L^\rho}{2} \mathbf{x}_{\mathbf{k}}$, where V is the volume. We note that this definition of PAM current corresponds to the conventional definition of spin current in the context of spin Hall effect [2], and similarly, it does not satisfy the continuity equation because $[\sigma^y L, H_{\mathbf{k}}] \neq 0$ [38, 40]. To compute the PAM Hall conductivity, we notice that the phonon Hamiltonian \mathcal{H} is a bosonic BdG Hamiltonian, as reviewed in SM [39]. Therefore, we can directly apply the linear response theory developed in Ref. [38] for a general bosonic BdG Hamiltonian: the expectation value of the PAM current to the linear order in the thermal gradient $\nabla_\nu T$ is given by $\langle j_\mu^{L^\rho} \rangle_{\text{neq}} = -\beta_{\mu\nu}^\rho \nabla_\nu T$, where

$$\beta_{\mu\nu}^\rho = \frac{k_B \hbar}{V} \sum_{\mathbf{k}} \sum_{n>0} \Omega_{\mu\nu,n}^\rho(\mathbf{k}) c_1(E_{\mathbf{k},n}), \quad (3)$$

$\Omega_{\mu\nu,n}^\rho(\mathbf{k}) = \sum_{m \neq n} \frac{\delta_{mm} \text{Im}[\langle n, \mathbf{k}|L^\rho v_{\mathbf{k},\mu} + v_{\mathbf{k},\mu} L^\rho|m, \mathbf{k}\rangle \langle m, \mathbf{k}|v_{\mathbf{k},\nu}|n, \mathbf{k}\rangle]}{(E_{\mathbf{k},n} - E_{\mathbf{k},m})^2}$, where $'$ indicates that the sum excludes $m = n$. Here, $v_{\mathbf{k},\mu} = \frac{1}{\hbar} \frac{\partial H_{\mathbf{k}}}{\partial k_\mu}$, $c_1(x) = (1 + g(x)) \log(1 + g(x)) - g(x) \log g(x)$, and $g(x) = \frac{1}{e^{x/k_B T} - 1}$ is the Bose-Einstein distribution. We show β_{xy}^z calculated for the square lattice model in Fig. 2 (b) (red line). We see that under the temperature gradient $(\nabla_y T)\hat{y}$ with $\nabla_y T > 0$, PAM flows in the $-\hat{x}$ direction, as heuristically argued previously. We also note that at $T = 100\text{K}$, the value of β_{xy}^z is about 10^4 times larger than the spin Nernst coefficient in Ref. [27] obtained for a hexagonal antiferromagnet.

We also notice that β_{xy}^z has a linear temperature dependence at low temperature in two dimensions. This is because $\Omega_{xy,n}^z(\mathbf{k}) \sim \frac{1}{k}$ [39], so that β_{xy}^z scales with temperature as $\int k^{d-2} dk c_1(g(\frac{vk}{k_B T})) \sim T^{d-1}$, where $d \geq 2$ is the spatial dimension and v is a constant (phonon velocity). Thus, for $d = 2$, $\beta_{xy}^z \propto T$, and for $d = 3$, $\beta_{xy}^z \propto T^2$.

Up to now, we have focused only on the in-plane phonon modes and disregarded the presence of out-of-plane phonon modes. In the case of square lattice, the out-of-plane modes and the in-plane modes do not mix because of the presence of the mirror symmetry $M_z : z \rightarrow -z$ about the lattice plane, so that β_{xy}^z does not change when we include the out-of-plane modes. On the other hand, when the symmetry is low enough, the out-of-plane modes may become important. In particular, β_{xy}^x and β_{xy}^y , which are not forbidden by the time reversal

and the inversion symmetries, may not vanish. We note, however, that in the case of square lattice, either of the mirror symmetries M_z or $M_x : x \rightarrow -x$ forbids β_{xy}^x , while M_z or $M_y : y \rightarrow -y$ forbids β_{xy}^y .

Let us also note that while we focus on $d = 2$ in this work, the theory can straightforwardly be extended to $d = 3$. To demonstrate this, we compute β_{xy}^z in a cubic lattice with NN and NNN longitudinal and transverse spring constants, similar to the case for square lattice. In accordance with the argument above, we observe that $\beta_{xy}^z \propto T^2$ at low temperature in Fig. 2 (b) (blue line).

Angular momentum accumulation— From the diffusion theory [8], we can expect accumulation of PAM at the edges proportional to the PAM lifetime and the PAM Hall current. For illustration, we calculate the PAM accumulation by introducing edges to the square lattice model. Let L_x^z be the PAM density of the atoms lying in the line along the y direction, passing through the position x , see Fig. 2 (c). The Boltzmann transport theory within constant relaxation time approximation gives [41] $g_{\text{neq}}(E) = g_{\text{eq}}(E) - \tau v \cdot \nabla T_\nu \frac{E}{k_B T^2} \frac{e^{E/k_B T}}{(e^{E/k_B T} - 1)^2}$. Thus, the part of the PAM density induced by temperature gradient $(\nabla_y T)\hat{y}$ which is proportional to the phonon lifetime τ is given by $\langle L_x^z \rangle_{\text{neq}} - \langle L_x^z \rangle_{\text{eq}} = -\lambda_y(x) \nabla T_y$, where

$$\lambda_y(x) = \frac{\tau}{2k_B T^2} \frac{1}{V} \sum_{\mathbf{k}} \sum_{n=-N}^N \langle n, \mathbf{k}|L_x^z|n, \mathbf{k}\rangle \times \langle n, \mathbf{k}|v_{\mathbf{k},y}|n, \mathbf{k}\rangle \frac{\delta_{nn} E_{\mathbf{k},n} e^{\delta_{nn} E_{\mathbf{k},n}/k_B T}}{(e^{\delta_{nn} E_{\mathbf{k},n}/k_B T} - 1)^2}. \quad (4)$$

We note that the same equation can be derived using the Kubo formula by making constant lifetime approximation and restricting to intraband contribution, as in Ref. [42].

Because PAM is not conserved, there is no simple correspondence between PAMHE and edge PAM accumulation [40]. Nevertheless, we obtain nontrivial edge PAM accumulation, as seen in Fig. 2 (c). Although the PAM is difficult to observe directly, if the atoms have nonzero Born effective charge Z_{eff} , the PAM will generate phonon magnetic moment (PMM) given by $\frac{e Z_{\text{eff}}}{2M} L^z$, where e is the elementary charge and M is the mass of the atom. Because the square lattice has only one atom per unit cell, we cannot expect the PAM to generate magnetization. We therefore consider next the checkerboard lattice.

Checkerboard lattice— Consider the checkerboard lattice in Fig. 3 (a) with two atoms A and B in a unit cell with mass M_A and $M_B = 1.5M_A$, respectively. Let the Born effective charge of A (B) be $Z_{\text{eff}}^A = 1$ ($Z_{\text{eff}}^B = -1$). In the phonon Hamiltonian, we include, as before, the longitudinal and transverse spring constants between the NN and the NNN. The energy spectrum is shown in Fig. 3 (b), where the values of the spring constants are given in the caption. The corresponding PAM Hall conductivity is shown in Fig. 3 (d) with black curve, which shows a similar behavior to Fig. 2 (b) (red curve) calculated for the square lattice.

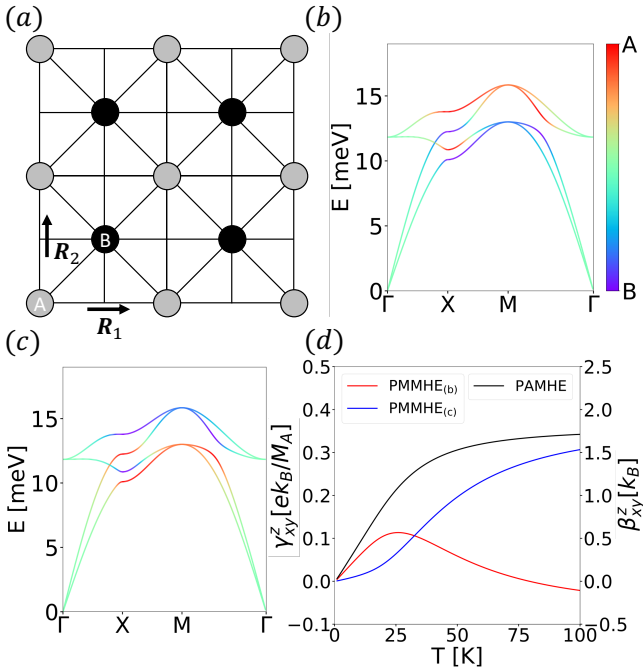


FIG. 3: (a) The checkerboard lattice, where the grey (black) circles indicate A (B) sites. (b) The energy spectrum with the NN transverse and longitudinal spring constants ($k_T = 20$ (meV) 2 and $k_L = 50$ (meV) 2) and the NNN transverse and longitudinal spring constants between the A sites ($k_T^A = 12$ (meV) 2 and $k_L^A = 30$ (meV) 2) and B sites ($k_T^B = 8$ (meV) 2 and $k_L^B = 20$ (meV) 2). The color represents the wavefunction content of A and B . (c) Energy spectrum and wavefunction content of A and B with the same parameters used for (b) except that the spring constant values between A and B sites are interchanged, i.e. $k_T^B = 12$ (meV) 2 , $k_L^B = 30$ (meV) 2 , $k_T^A = 8$ (meV) 2 , and $k_L^A = 20$ (meV) 2 . (d) The PMM Hall conductivities for the parameters in (b) (red curve) and (c) (blue curve) and the PAM Hall conductivity (black curve).

Because $Z_{\text{eff}}^{A,B} \neq 0$ for the atoms in the checkerboard lattice, we can define the PMM Hall effect (PMMHE) in addition to the PAMHE, wherein the temperature gradient causes a transverse flow of PMM. The PMM Hall conductivity γ_{xy}^z , which is defined in the same way as PAM Hall conductivity by replacing L_α^z by $\mu_\alpha L_\alpha^z$ with $\mu_\alpha = \frac{Z_{\text{eff}}^\alpha e}{2M_\alpha}$ for $\alpha = A, B$, shows a very different behavior, as can be seen in Fig. 3 (d) (red curve).

In order to understand this behavior, we notice that the spring constants between the A sites are stiffer than between the B sites, $\mu_A \cdot \mu_B < 0$, and $\mu_A > |\mu_B|$. In addition, for energy less than approximately 5 meV, the phonon wavefunction is nearly equally shared between the A and the B sites, as can be seen in Fig. 3 (b). However, the PAM arising from A sites is expected to be transported faster than PAM arising from B sites because the spring constants between A sites are stiffer than those between B sites. Thus, γ_{xy}^z shown in Fig. 3 (d) (red curve) has the same sign as β_{xy}^z at low temperature because the contribution to γ_{xy}^z from the A sites with positive Born effective charge is larger. However, at higher energy,

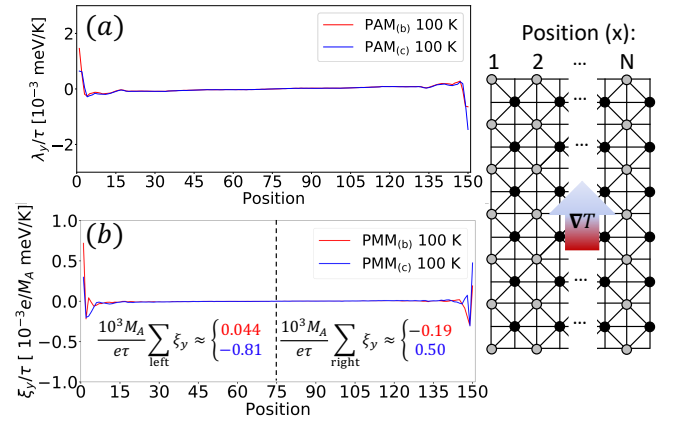


FIG. 4: (a) PAM accumulation with the configuration shown on the right. The red and the blue lines are calculated with the parameters in Fig. 3 (b) and (c) respectively. (b) PMM accumulation, where the red and the blue lines are calculated with the parameters in Fig. 3 (b) and (c) respectively. The sum of $\frac{10^3 M_A}{e\tau} \xi_y$ for the left half of the system is 0.044 meV/K (-0.81 meV/K) for the red (blue) curve, and the sum for the right half of the system is -0.19 meV/K (0.50 meV/K) for the red (blue) curve.

B sites have significantly higher occupation so that γ_{xy}^z decreases with increasing temperature, and even change sign, since the contribution to γ_{xy}^z from B sites with negative Born effective charge significantly increases.

To gain a deeper understanding of the behavior of γ_{xy}^z , it is convenient to interchange the values of the NNN spring constants between the A and those between the B sites. Under this operation, the energy spectrum and β_{xy}^z remain the same as before, while the wavefunction contents of A and B sites switch, as can be seen in Fig. 3 (c) [39]. Unlike β_{xy}^z , the behavior of γ_{xy}^z is very different, as can be seen in Fig. 3 (d) (blue curve). To explain this, note that for energy approximately less than 5 meV, the wavefunction is nearly equally shared between A and B , while the spring constants between the B sites are stiffer than those between A sites. Therefore, the PAM arising from B sites are transported faster, so that γ_{xy}^z is smaller than that obtained previously at low temperature, although we still have $\gamma_{xy}^z > 0$ because $\mu_A > |\mu_B|$. At higher energy, the wavefunction content is higher for A sites, so that the value of γ_{xy}^z keeps increasing with temperature.

To illustrate the implications of the PAM and PMM Hall currents, we compute the spatial distribution of PAM $\lambda_y(x)$ in Eq.(4), and that of PMM $\xi_y(x)$, which is defined in the same way as $\lambda_y(x)$ by replacing L_α^z with $\mu_\alpha L_\alpha^z$. Note that two lines of atoms, each consisting of either A or B , are contained in a single position index, as shown in Fig. 4. We show $\lambda_y(x)$ and $\xi_y(x)$ in Fig. 4 (a) and (b) respectively, computed using the two sets of parameters discussed above, which were used in Fig. 3 (b) and (c), respectively. In Fig. 4 (a), we see that the spatial distribution of PAM does not differ much between the two sets of parameters, which is not surprising as the two cases show the same PAM Hall conductivity. However, the

different behaviors of PMM Hall conductivity γ_{xy}^z in Fig. 3 (d) for the two sets of parameters foretell different behaviors for the distribution of PMM, which we show in Fig. 4 (b). We find that the PMM accumulation at the left and the right edges are nearly balanced out for the red curve in Fig. 4 (b), whereas there is a significant asymmetry in the blue curve, which is in accordance with the behavior of γ_{xy}^z in Fig. 3 (d). We further note that the induced PMM near the edges has order of magnitude of $\tau/(1s)$ Bohr magneton per unit cell for the blue curve, where we have assumed that the unit cell size is 5\AA , M_A is 25 amu, and the temperature gradient is $10\text{K}/100\mu\text{m}$. If we assume that the acoustic phonon lifetime is $10 \sim 100$ ps [43], the PMM accumulation can be expected to be around $10^{-11} \sim 10^{-10}$ Bohr magneton per unit cell. This value is similar to the bulk PMM induced by the thermal analog of Edelstein effect obtained in Ref. [33] for GaN.

Discussion— We have shown that the PAMHE occurs ubiquitously whenever there are longitudinal and transverse phonon modes. Moreover, we can expect PAM Hall conductivity to behave similarly in different systems through the heuristic argument given in the introduction. In contrast, the behavior of PMMHE is not universal, but we can expect it to be sizable in ionic crystals if the masses of the ions with opposite charge differ significantly.

We have also shown that the PAM and PMM Hall currents induce edge PAM and PMM accumulation. Because the PMM Hall current induces PMM accumulation, it can make significant contribution to edge magnetization other than that from magnon spin Nernst effect in thermal transport experiments of magnetic insulators. Since both the phonon and magnon degrees of freedom are important in magnetic insulators, this also brings up the question of the role of spin-phonon interaction on the transport of the magnon spin and the PAM, especially since spin-phonon interaction may significantly modify the PAM [31], which we leave for future study.

S.P. thanks H.-W. Lee for giving an enlightening talk at MSM19, which motivated this work. S.P. was supported by IBS-R009-D1. B.-J.Y. was supported by the Institute for Basic Science in Korea (Grant No. IBS-R009-D1) and Basic Science Research Program through the National Research Foundation of Korea (NRF) (Grant No. 0426-20190008), and the POSCO Science Fellowship of POSCO TJ Park Foundation (No. 0426-20180002). This work was supported in part by the U.S. Army Research Office under Grant Number W911NF-18-1-0137.

* Electronic address: bjyang@snu.ac.kr

[1] N. Nagaosa, J. Sinova, S. Onoda, A. H. MacDonald, and N. P. Ong, *Rev. Mod. Phys.* **82**, 1539 (2010).
 [2] J. Sinova, S. O. Valenzuela, J. Wunderlich, C. Back, and T. Jungwirth, *Rev. Mod. Phys.* **87**, 1213 (2015).
 [3] R. Karplus and J. Luttinger, *Phys. Rev.* **95**, 1154 (1954).
 [4] J. Smit, *Physica* **24**, 39 (1958).
 [5] L. Berger, *Phys. Rev. B* **2**, 4559 (1970).

[6] M. D'yakonov and V. Perel, *JETP Lett.* **13**, 467 (1971).
 [7] J. Hirsch, *Phys. Rev. Lett.* **83**, 1834 (1999).
 [8] S. Murakami, N. Nagaosa, and S.-C. Zhang, *Science* **301**, 1348 (2003).
 [9] J. Sinova, D. Culcer, Q. Niu, N. Sinitsyn, T. Jungwirth, and A. H. MacDonald, *Phys. Rev. Lett.* **92**, 126603 (2004).
 [10] Y. K. Kato, R. C. Myers, A. C. Gossard, and D. D. Awschalom, *Science* **306**, 1910 (2004).
 [11] J. Wunderlich, B. Kaestner, J. Sinova, and T. Jungwirth, *Phys. Rev. Lett.* **94**, 047204 (2005).
 [12] B. A. Bernevig, T. L. Hughes, and S.-C. Zhang, *Phys. Rev. Lett.* **95**, 066601 (2005).
 [13] F. D. M. Haldane, *Phys. Rev. Lett.* **61**, 2015 (1988).
 [14] C. L. Kane and E. J. Mele, *Phys. Rev. Lett.* **95**, 226801 (2005).
 [15] C. L. Kane and E. J. Mele, *Phys. Rev. Lett.* **95**, 146802 (2005).
 [16] R. Popović, *Sensors and Actuators* **17**, 39 (1989).
 [17] T. Jungwirth, J. Wunderlich, and K. Olejník, *Nat. Mater.* **11**, 382 (2012).
 [18] H. Katsura, N. Nagaosa, and P. A. Lee, *Phys. Rev. Lett.* **104**, 066403 (2010).
 [19] Y. Onose, T. Ideue, H. Katsura, Y. Shiomi, N. Nagaosa, and Y. Tokura, *Science* **329**, 297 (2010).
 [20] R. Matsumoto and S. Murakami, *Phys. Rev. Lett.* **106**, 197202 (2011).
 [21] C. Strohm, G. Rikken, and P. Wyder, *Phys. Rev. Lett.* **95**, 155901 (2005).
 [22] L. Sheng, D. Sheng, and C. Ting, *Phys. Rev. Lett.* **96**, 155901 (2006).
 [23] Y. Kagan and L. Maksimov, *Phys. Rev. Lett.* **100**, 145902 (2008).
 [24] L. Zhang, J. Ren, J.-S. Wang, and B. Li, *Phys. Rev. Lett.* **105**, 225901 (2010).
 [25] S. Park and B.-J. Yang, *Phys. Rev. B* **99**, 174435 (2019).
 [26] X. Zhang, Y. Zhang, S. Okamoto, and D. Xiao, *Phys. Rev. Lett.* **123**, 167202 (2019).
 [27] R. Cheng, S. Okamoto, and D. Xiao, *Phys. Rev. Lett.* **117**, 217202 (2016).
 [28] V. A. Zyuzin and A. A. Kovalev, *Phys. Rev. Lett.* **117**, 217203 (2016).
 [29] S. Park, N. Nagaosa, and B.-J. Yang, *arXiv preprint arXiv:1910.07206* (2019).
 [30] S. Zhang, G. Go, K.-J. Lee, and S. K. Kim, *arXiv preprint arXiv:1909.08031* (2019).
 [31] L. Zhang and Q. Niu, *Phys. Rev. Lett.* **112**, 085503 (2014).
 [32] D. M. Juraschek, M. Fechner, A. V. Balatsky, and N. A. Spaldin, *Phys. Rev. Mater.* **1**, 014401 (2017).
 [33] M. Hamada, E. Minamitani, M. Hirayama, and S. Murakami, *Phys. Rev. Lett.* **121**, 175301 (2018).
 [34] D. M. Juraschek and N. A. Spaldin, *Phys. Rev. Mater.* **3**, 064405 (2019).
 [35] D. Go, D. Jo, C. Kim, and H.-W. Lee, *Phys. Rev. Lett.* **121**, 086602 (2018).
 [36] J. Luttinger, *Phys. Rev.* **135**, A1505 (1964).
 [37] R. Matsumoto, R. Shindou, and S. Murakami, *Phys. Rev. B* **89**, 054420 (2014).
 [38] B. Li, S. Sandhoefner, and A. A. Kovalev, *arXiv preprint arXiv:1907.10567* (2019).
 [39] Supplemental Material.
 [40] J. Shi, P. Zhang, D. Xiao, and Q. Niu, *Phys. Rev. Lett.* **96**, 076604 (2006).
 [41] N. W. Ashcroft and N. D. Mermin, *Solid State Physics* (New York: Holt, Rinehart and Winston, 1976).
 [42] A. Mook, R. R. Neumann, J. Henk, and I. Mertig, *arXiv preprint arXiv:1903.11896* (2019).

- [43] A. Togo, L. Chaput, and I. Tanaka, *Phys. Rev. B* **91**, 094306 (2015).

Angular momentum of shifted states

Recall that the equation of motion for the normal modes $\sigma^y H_{\mathbf{k}} \chi_{\mathbf{k},n} = E_{\mathbf{k},n} \chi_{\mathbf{k},n}$ in the continuum model yields

$$\chi_{\mathbf{k},n} = \begin{pmatrix} -iE_{\mathbf{k},n} \epsilon_{\mathbf{k},n} \\ \epsilon_{\mathbf{k},n} \end{pmatrix} \quad (5)$$

where

$$E_{\mathbf{k},L} = -E_{\mathbf{k},-L} = v_L k \quad (6)$$

$$E_{\mathbf{k},T} = -E_{\mathbf{k},-T} = v_T k \quad (7)$$

$$\epsilon_{\mathbf{k},L} = \epsilon_{\mathbf{k},-L} = \frac{1}{k\sqrt{2E_{\mathbf{k},L}}} \begin{pmatrix} k_x \\ k_y \end{pmatrix} \quad (8)$$

$$\epsilon_{\mathbf{k},T} = \epsilon_{\mathbf{k},-T} = \frac{1}{k\sqrt{2E_{\mathbf{k},T}}} \begin{pmatrix} k_y \\ -k_x \end{pmatrix} \quad (9)$$

It can be checked that the normalization condition $\chi_{\mathbf{k},m}^\dagger \sigma^y \chi_{\mathbf{k},n} = \delta_{mn}$ is satisfied. Also, the expression $\mathcal{L}^z = \frac{1}{2} \sum_{\mathbf{k},m,n} \langle m, \mathbf{k} | L^z | n, \mathbf{k} \rangle b_{\mathbf{k},m}^\dagger b_{\mathbf{k},n}$ given in the main text shows that the angular momentum of the longitudinal and transverse modes are given respectively by $\langle L, \mathbf{k} | L^z | L, \mathbf{k} \rangle$ and $\langle T, \mathbf{k} | L^z | T, \mathbf{k} \rangle$, where the properties $b_{\mathbf{k},n}^\dagger = b_{-\mathbf{k},-n}$ and $|-n, -\mathbf{k}\rangle = \mathcal{X} |n, \mathbf{k}\rangle$ were used to eliminate the (redundant) negative-energy modes.

Below, we show that the transverse mode with momentum shift $\mathbf{k} \rightarrow \mathbf{k}' = \mathbf{k} + \delta\mathbf{k}$, $\chi_{\mathbf{k},T}^{\text{shift}}(t) = \sum_n e^{-itE_{\mathbf{k}',n}} \alpha_n^T \chi_{\mathbf{k}',n}$, develops angular momentum $\langle \mathcal{L}^z \rangle_{\mathbf{k},T}^{\text{shift}}(t) = (\chi_{\mathbf{k},T}^{\text{shift}})^\dagger(t) L^z \chi_{\mathbf{k},T}^{\text{shift}}(t) \propto -k_x \delta k_y t$, to linear order in t . For this, it is useful to note that since $\chi_{\mathbf{k},n}^\dagger L^z \chi_{\mathbf{k},n} = 0$, only cross terms between $\chi_{\mathbf{k},n}$ can appear in $\langle \mathcal{L}^z \rangle_{\mathbf{k},T}^{\text{shift}}(t)$. Also, by noting that

$$\begin{aligned} \epsilon_{\mathbf{k}',L} \cdot \epsilon_{\mathbf{k},T} &= \frac{k_x \delta k_y}{k^2 \sqrt{4E_{\mathbf{k}',L} E_{\mathbf{k},T}}} \\ \epsilon_{\mathbf{k}',T} \cdot \epsilon_{\mathbf{k},T} &= \frac{k^2 - k_y \delta k_y}{k^2 \sqrt{4E_{\mathbf{k}',T} E_{\mathbf{k},T}}} \end{aligned} \quad (10)$$

we have

$$\begin{aligned} \alpha_L^T &= (E_{\mathbf{k}',L} + E_{\mathbf{k},T}) \epsilon_{\mathbf{k}',L} \cdot \epsilon_{\mathbf{k},T} \propto \delta k_y \\ \alpha_T^T &= (E_{\mathbf{k}',T} + E_{\mathbf{k},T}) \epsilon_{\mathbf{k}',T} \cdot \epsilon_{\mathbf{k},T} \propto (\delta k_y)^0 \\ \alpha_{-L}^T &= -(-E_{\mathbf{k}',L} + E_{\mathbf{k},T}) \epsilon_{\mathbf{k}',L} \cdot \epsilon_{\mathbf{k},T} \propto \delta k_y \\ \alpha_{-T}^T &= -(-E_{\mathbf{k}',T} + E_{\mathbf{k},T}) \epsilon_{\mathbf{k}',T} \cdot \epsilon_{\mathbf{k},T} \propto \delta k_y. \end{aligned} \quad (11)$$

Thus, to the lowest order in δk_y ,

$$\begin{aligned} \langle \mathcal{L}^z \rangle_{\mathbf{k},T}^{\text{shift}}(t) &= 2\text{Re}[\alpha_L^T \alpha_T^T e^{it(E_{\mathbf{k}',L} - E_{\mathbf{k},T})} \chi_{\mathbf{k}',L}^\dagger L^z \chi_{\mathbf{k},T} \\ &\quad + \alpha_T^T \alpha_{-L}^T e^{it(E_{\mathbf{k}',T} + E_{\mathbf{k},L})} \chi_{\mathbf{k}',T}^\dagger L^z \chi_{\mathbf{k},-L}] \end{aligned} \quad (12)$$

Together with

$$\begin{aligned} \chi_{\mathbf{k}',L}^\dagger L^z \chi_{\mathbf{k},T} &= \frac{i(E_{\mathbf{k}',L} + E_{\mathbf{k},T})}{\sqrt{4E_{\mathbf{k}',L} E_{\mathbf{k},T}}} \\ \chi_{\mathbf{k}',T}^\dagger L^z \chi_{\mathbf{k},-L} &= \frac{-i(E_{\mathbf{k}',T} - E_{\mathbf{k},L})}{\sqrt{4E_{\mathbf{k}',L} E_{\mathbf{k},T}}} \end{aligned} \quad (13)$$

and Eqs. (10) and (11), we see that to the lowest order in t and δk_y , $\langle \mathcal{L}^z \rangle_{\mathbf{k},T}^{\text{shift}}(t) \propto -k_x \delta k_y t$ with positive coefficients when $v_L > v_T$. Note that the proportionality to t follows by Taylor expanding the exponential factors. Similarly, we can show that $\langle \mathcal{L}^z \rangle_{\mathbf{k},L}^{\text{shift}}(t) \propto k_x \delta k_y t$ with positive coefficients when $v_L > v_T$.

Details of the models

Define the nearest neighbor spring constant matrix as

$$K(\mathbf{R}_1) = \begin{pmatrix} -k_L & 0 \\ 0 & -k_T \end{pmatrix}, \quad K(\mathbf{R}_2) = \begin{pmatrix} -k_T & 0 \\ 0 & -k_L \end{pmatrix}. \quad (14)$$

Then, the onsite potential is given by

$$K^{nn}(0) = 2 \begin{pmatrix} k_L + k_T & 0 \\ 0 & k_L + k_T \end{pmatrix}. \quad (15)$$

The dynamical matrix for the nearest neighbors is given by

$$D_{\mathbf{k}}^{nn} = K^{nn}(0) + 2K(\mathbf{R}_1) \cos k_x + 2K(\mathbf{R}_2) \cos k_y. \quad (16)$$

For nontrivial polarization vectors, we also need the next nearest neighbor spring constants, which are given as

$$\begin{aligned} K(\mathbf{R}_1 + \mathbf{R}_2) &= C\left(\frac{\pi}{4}\right) \begin{pmatrix} -k'_L & 0 \\ 0 & -k'_T \end{pmatrix} C^T\left(\frac{\pi}{4}\right) \\ &= -\frac{1}{2} \begin{pmatrix} k'_L + k'_T & k'_L - k'_T \\ k'_L - k'_T & k'_L + k'_T \end{pmatrix} \end{aligned} \quad (17)$$

and

$$\begin{aligned} K(\mathbf{R}_1 - \mathbf{R}_2) &= C^T\left(\frac{\pi}{4}\right) \begin{pmatrix} -k'_L & 0 \\ 0 & -k'_T \end{pmatrix} C\left(\frac{\pi}{4}\right) \\ &\quad - \frac{1}{2} \begin{pmatrix} k'_L + k'_T & -k'_L + k'_T \\ -k'_L + k'_T & k'_L + k'_T \end{pmatrix}, \end{aligned} \quad (18)$$

where $C(\frac{\pi}{4})$ is the rotation matrix by $\frac{\pi}{4}$ in the counterclockwise direction. The onsite potential is

$$K^{nnn}(0) = 2 \begin{pmatrix} k'_L + k'_T & 0 \\ 0 & k'_L + k'_T \end{pmatrix}. \quad (19)$$

The dynamical matrix for next nearest neighbors is given by

$$\begin{aligned} D_{\mathbf{k}}^{nnn} &= K^{nnn}(0) + 2K(\mathbf{R}_1 + \mathbf{R}_2) \cos(k_x + k_y) \\ &\quad + 2K(\mathbf{R}_1 - \mathbf{R}_2) \cos(k_x - k_y). \end{aligned} \quad (20)$$

A similar analysis can be carried out for the cubic lattice by replacing, for example, $K(\mathbf{R}_1)$ in Eq. (14) by

$$K(\mathbf{R}_1) = \begin{pmatrix} -k_L & 0 & 0 \\ 0 & -k_T & 0 \\ 0 & 0 & -k_T \end{pmatrix}. \quad (21)$$

In the case of checkerboard lattice, we have two sites, A and B , per unit cell. Define $\delta_A = 0$, $\delta_B = \frac{\mathbf{R}_1 + \mathbf{R}_2}{2}$, $\delta'_B = \frac{\mathbf{R}_1 - \mathbf{R}_2}{2}$. Then,

$$K(\delta_B) = -\frac{1}{2} \begin{pmatrix} k_L + k_T & k_L - k_T \\ k_L - k_T & k_L + k_T \end{pmatrix}, \quad (22)$$

while the other nearest neighbor spring constant matrices can be obtained by imposing the fourfold rotation symmetry. The next nearest neighbor spring constant matrices are

$$K^\alpha(\mathbf{R}_1) = \begin{pmatrix} -k_L^\alpha & 0 \\ 0 & -k_T^\alpha \end{pmatrix}, \quad K^\alpha(\mathbf{R}_2) = \begin{pmatrix} -k_T^\alpha & 0 \\ 0 & -k_L^\alpha \end{pmatrix}, \quad (23)$$

where $\alpha = A$ or B , and the onsite potential is obtained by demanding that there is no energy cost in uniform translation of the lattice: $K_{nn}^\alpha = -K(\boldsymbol{\delta}_B) - K(\boldsymbol{\delta}'_B)$, and $K_{nnn}^\alpha = -2K^\alpha(\mathbf{R}_1) - 2K^\alpha(\mathbf{R}_2)$. The dynamical matrix takes the form

$$D_{\mathbf{k}} = \begin{pmatrix} D_{\mathbf{k}}^A & D_{\mathbf{k}}^{AB} \\ D_{\mathbf{k}}^{AB} & D_{\mathbf{k}}^B \end{pmatrix}, \quad (24)$$

where $D_{\mathbf{k}}^\alpha = K_{nn}^\alpha + K_{nnn}^\alpha + 2K^\alpha(\mathbf{R}_1) \cos k_x + 2K^\alpha(\mathbf{R}_2) \cos k_y$ and $D_{\mathbf{k}}^{AB} = K(\boldsymbol{\delta}_B) \cos \frac{k_x + k_y}{2} + K(\boldsymbol{\delta}'_B) \cos \frac{k_x - k_y}{2}$. It is easy to see that the process of interchanging $k_L^A, k_T^A \leftrightarrow k_L^B, k_T^B$ is equivalent to the transformation $D_{\mathbf{k}} \rightarrow D'_{\mathbf{k}} = I_{AB} D_{\mathbf{k}} I_{AB}^\dagger$, where

$$I_{AB} = \begin{pmatrix} 0 & I_2 \\ I_2 & 0 \end{pmatrix} \quad (25)$$

and I_2 is the two by two identity matrix. Thus, if $D_{\mathbf{k}} \boldsymbol{\epsilon}_{\mathbf{k},n} = E_{\mathbf{k},n}^2 \boldsymbol{\epsilon}_{\mathbf{k},n}$, $D'_{\mathbf{k}} \boldsymbol{\epsilon}'_{\mathbf{k},n} = E_{\mathbf{k},n}^2 \boldsymbol{\epsilon}'_{\mathbf{k},n}$, where $\boldsymbol{\epsilon}'_{\mathbf{k},n} = I_{AB} \boldsymbol{\epsilon}_{\mathbf{k},n}$. Thus, under the interchange of the spring constant values, the energy spectrum is not changed in any way. Noting that the phonon wavefunction is given by $\boldsymbol{\chi}_{\mathbf{k},n} = \begin{pmatrix} -iE_{\mathbf{k},n} \boldsymbol{\epsilon}_{\mathbf{k},n} \\ \boldsymbol{\epsilon}_{\mathbf{k},n} \end{pmatrix}$, we see that the wavefunction content of A and B are interchanged.

Transformation to BdG basis

From the field operator $\mathbf{x}_{\mathbf{k}} = \begin{pmatrix} p_{\mathbf{k}} \\ u_{\mathbf{k}} \end{pmatrix}$, we can obtain the bosonic BdG field operators $\mathbf{y}_{\mathbf{k}}$ by making the transformation $\mathbf{y}_{\mathbf{k}} = \frac{\sqrt{2}}{2} \begin{pmatrix} p_{\mathbf{k}} - iu_{\mathbf{k}} \\ p_{\mathbf{k}} + iu_{\mathbf{k}} \end{pmatrix} = U \mathbf{x}_{\mathbf{k}}$. Then, $[y_{\mathbf{k},i}^\dagger, y_{\mathbf{k}',j}] = -\delta_{i,j} \delta_{\mathbf{k},\mathbf{k}'}$ and $y_{\mathbf{k},i}^\dagger = \sum_j \sigma_{ij}^x y_{-\mathbf{k},j}$ (here, $\delta_{i,j} = 1$ if $i = j$ and 0 otherwise). Making the same transformation to the eigenvectors $\boldsymbol{\xi}_{\mathbf{k},n} = U \boldsymbol{\chi}_{\mathbf{k},n}$, we have $\sigma^z H_{\mathbf{k}} \boldsymbol{\xi}_{\mathbf{k},n} = E_{\mathbf{k},n} \boldsymbol{\xi}_{\mathbf{k},n}$ and $\boldsymbol{\xi}_{\mathbf{k},m}^\dagger \sigma^z \boldsymbol{\xi}_{\mathbf{k},n} = \delta_{mn}$ [25]. It is convenient to know that this relation exists between the phonon and bosonic BdG Hamiltonian, as the expressions for the transport coefficients calculated for a general bosonic BdG Hamiltonian can directly be applied to phonon Hamiltonian as well.

Commutator between \mathcal{L} and \mathcal{H}

First, we note that $[x_{km}, x_{k'n}] = -\sigma_{mn}^y \delta_{\mathbf{k},-\mathbf{k}'}$, $\mathcal{L} = \frac{1}{2} \sum_{\mathbf{k}} \mathbf{x}_{-\mathbf{k}} L \mathbf{x}_{\mathbf{k}}$, $\mathcal{H} = \frac{1}{2} \sum_{\mathbf{k}} \mathbf{x}_{-\mathbf{k}} H_{\mathbf{k}} \mathbf{x}_{\mathbf{k}}$, and $H_{\mathbf{k}} = H_{-\mathbf{k}}^T$.

We find

$$\begin{aligned} [\mathcal{L}, \mathcal{H}] &= \frac{1}{4} \sum_{\mathbf{k}} \mathbf{x}_{-\mathbf{k}} [H_{\mathbf{k}} i\sigma^y L + H_{-\mathbf{k}}^T i\sigma^y L \\ &\quad - i\sigma^y L H_{\mathbf{k}} - i\sigma^y L H_{-\mathbf{k}}^T] \mathbf{x}_{\mathbf{k}} \\ &= \frac{1}{2} \sum_{\mathbf{k}} \mathbf{x}_{-\mathbf{k}} [H_{\mathbf{k}}, i\sigma^y L] \mathbf{x}_{\mathbf{k}}. \end{aligned} \quad (26)$$

Since $[H_{\mathbf{k}}, i\sigma^y L] \neq 0$ in general, which can easily be checked for all of the models we have used in this work, phonon angular momentum is not conserved. In the (point) mass and spring model, the conserved operator is $\mathcal{L}^{tot} = \sum_{\mathbf{R},\alpha} r_\alpha(\mathbf{R}) \times \mathbf{p}_\alpha(\mathbf{R})$, where $r_\alpha(\mathbf{R}) = \mathbf{R} + \boldsymbol{\delta}_\alpha + \mathbf{u}_\alpha(\mathbf{R})$, so that the phonon angular momentum can be converted to $\mathcal{L}^{lat} = \sum_{\mathbf{R},\alpha} (\mathbf{R} + \boldsymbol{\delta}_\alpha) \times \mathbf{p}_\alpha(\mathbf{R})$. If we also include the electronic degrees of freedom, the conserved total angular momentum should also include the spin and orbital degrees of freedom.

Temperature dependence of βz_y

At low energy, the dynamical matrix of our square lattice model can be approximated as

$$D_{\mathbf{k}} = d_0 \mathbf{k}^2 \tau_0 + d_z (k_x^2 - k_y^2) \tau_z + d_x k_x k_y \tau_x, \quad (27)$$

where the coefficients are $d_0 = \frac{k_L + k_T}{2} + k'_L + k'_T$, $d_x = 2(k'_L - k'_T)$, and $d_z = \frac{k_L - k_T}{2}$ and τ_μ for $\mu = x, y, z$ are the two-by-two Pauli matrices. The (unit normalized) eigenvectors and eigenvalues of matrix of the form $a\tau_x + b\tau_z$ are given by

$$u_\pm = \frac{1}{\sqrt{2c(c \mp b)}} \begin{pmatrix} a \\ -b \pm c \end{pmatrix}, \quad c = \sqrt{a^2 + b^2}, \quad (28)$$

which can be used to immediately obtain the polarization vectors and the energy. In general, the polarization vectors near the Γ point are not exactly longitudinal or transverse. However, in the special case where $d_x = 2d_z$, the polarization vectors are longitudinal and transverse polarized.

For simplicity, we will analytically study only this case, which does not affect the generality of the result. The dynamical matrix is given by

$$D_{\mathbf{k}} = \begin{pmatrix} v_L^2 k_x^2 + v_T^2 k_y^2 & (v_L^2 - v_T^2) k_x k_y \\ (v_L^2 - v_T^2) k_x k_y & v_T^2 k_x^2 + v_L^2 k_y^2 \end{pmatrix}. \quad (29)$$

The energy of the longitudinal and transverse modes are

$$E_L = v_L k, \quad E_T = v_T k \quad (30)$$

with polarization vectors (normalized using the convention given in the main text)

$$\boldsymbol{\epsilon}_L = \frac{1}{\sqrt{2v_L k^{3/2}}} \begin{pmatrix} k_x \\ k_y \end{pmatrix}, \quad \boldsymbol{\epsilon}_T = \frac{1}{\sqrt{2v_T k^{3/2}}} \begin{pmatrix} k_y \\ -k_x \end{pmatrix}. \quad (31)$$

Omitting the momentum space sector, which are zero, the velocity operators are

$$\begin{aligned} v_x &= \begin{pmatrix} 2v_L^2 k_x & (v_L^2 - v_T^2)k_y \\ (v_L^2 - v_T^2)k_y & 2v_T^2 k_x \end{pmatrix} \\ v_y &= \begin{pmatrix} 2v_T^2 k_y & (v_L^2 - v_T^2)k_x \\ (v_L^2 - v_T^2)k_x & 2v_L^2 k_y \end{pmatrix}. \end{aligned} \quad (32)$$

Recalling the definition of $\Omega_{\mu\nu,n}^z(\mathbf{k})$, defined below Eq. (3) of the main text, we find

$$\begin{aligned} \Omega_{xy,L}^z(\mathbf{k}) &= -\frac{k_y^2(v_L^2 - v_T^2)^2 + 4k_x^2(v_L^4 + 3v_L^2 v_T^2)}{4k^3 v_L(v_L^2 - v_T^2)} \\ \Omega_{yx,L}^z(\mathbf{k}) &= \frac{k_x^2(v_L^2 - v_T^2)^2 + 4k_y^2(v_L^4 + 3v_L^2 v_T^2)}{4k^3 v_L(v_L^2 - v_T^2)} \\ \Omega_{xy,T}^z(\mathbf{k}) &= -\frac{k_y^2(v_L^2 - v_T^2)^2 + 4k_x^2(v_T^4 + 3v_L^2 v_T^2)}{4k^3 v_T(v_T^2 - v_L^2)} \\ \Omega_{yx,T}^z(\mathbf{k}) &= \frac{k_x^2(v_L^2 - v_T^2)^2 + 4k_y^2(v_T^4 + 3v_L^2 v_T^2)}{4k^3 v_T(v_T^2 - v_L^2)}. \end{aligned} \quad (33)$$

The point is that $\Omega_{\mu\nu,n}^z(\mathbf{k}) \sim \frac{1}{k}$ for $n = L, T$, so that $\beta_{\mu\nu}^z \sim \int dk c_1(g(\frac{vk}{k_B T})) \sim T$ has a linear temperature dependence. In three dimensions, we still have $\Omega_{xy,n}^z(\mathbf{k}) \sim \frac{1}{k}$ so that $\beta_{xy}^z \sim \int dk k c_1(g(\frac{vk}{k_B T}))$ has quadratic temperature dependence.

Using Eq. (33), we can also show that even though both $\Omega_{xy,L}^z(\mathbf{k})$ and $\Omega_{xy,T}^z(\mathbf{k})$ diverge as v_L and v_T approach each other, their sign is opposite so that the divergence cancels in β_{xy}^z . We can similarly show that the quadratic band crossing at the M point in the energy spectrum of the square-lattice model does not cause any divergence in β_{xy}^z .